Science Advances
◣AAAS

Supplementary Materials for

Resonant nanodiffraction x-ray imaging reveals role of magnetic domains in complex oxide spin caloritronics

Paul G. Evans*, Samuel D. Marks, Stephan Geprägs, Maxim Dietlein, Yves Joly, Minyi Dai, Jiamian Hu, Laurence Bouchenoire, Paul B. J. Thompson, Tobias U. Schülli, Marie-Ingrid Richard, Rudolf Gross, Dina Carbone, Danny Mannix

*Corresponding author. Email: pgevans@wisc.edu

This PDF file includes:

Supplementary Text
Figs. S1 to S4
References

Supplementary Text

Incident x-ray beam preparation and polarization characterization. The incident x-ray beam was prepared in a specified polarization using a diamond phase plate (*28*). The x-ray phase plate consisted of a diamond crystal with a nominal thickness t=800 μm and a [110] surface normal, mounted at an angle of 45° so that there were equal projections of the incident horizontal x-ray polarization onto the σ and π polarizations of the diffracting diamond planes. The plate was set with an angular orientation with respect to the incident beam such that the diamond (111) planes were misoriented by 54.74° with respect to the plane of the surface with diffraction in a Laue diffraction geometry. The effective thickness of the crystal at Bragg angle θ_B was thus t_{eff}=t/sin(35.26°+θ_B).

The phase shift δ between the two orthogonal linear components of the x-ray beam for when the diamond is misoriented by Δθ with respect to the Bragg condition is given by (*28*):

$$\delta = \frac{r_e^2 \lambda^3 t_{eff}}{2\pi V^2} \frac{\sin(2\theta_B) \, Re(F^+F^-)}{} \frac{1}{\Delta\theta}$$

Here r_e is the classical radius of the electron, λ is the x-ray wavelength, F^+ and F^- are the structure factors of the diamond 111 and $\overline{1}\,\overline{1}\,\overline{1}$ reflections, and V is the volume of the diamond unit cell. The vector sum of the two linear components produces an altered transmitted polarization depending on the value of δ.

The transmitted beam polarization is described by the Poincaré coefficients for circular and linear polarization, P_c and P_L (*28*):

$$P_c = \sin(\delta) \tag{1a}$$
$$P_L = \cos(\delta) \tag{1b}$$

The polarization of the incident x-ray beam was characterized by measuring and normalizing the intensities I_H and I_V of the horizontally and vertically polarized components of the beam. These intensities were measured using scattering to 90 degrees in the vertical and horizontal directions, respectively. The Poincaré coefficients were determined from the intensities using (*28, 42*):

$$P_L = \frac{I_H - I_V}{I_H + I_V}$$

$$|P_c| = (1 - P_L{}^2)^{1/2}$$

This approach does not allow the sign of P_c to be determined.

The measured and predicted values of the P_L and P_c are shown in Figs. S1(a) and S1(b). The measured curve accurately follows the prediction. There are two notable artifacts in analysis shown in Fig. S1:

(1) The intensities I_H and I_V were measured using polyimide foils mounted at 45° with respect to the beam and scattering in the horizontal and vertical directions, respectively. The intensities were not measured on an absolute scale and were thus normalized with respect to the maxima and minima of each signal, respectively. This approach likely introduces an artificially large value of the linear polarization P_L because the value of I_V is underestimated at its minimum.

(2) The prediction does not account for the finite angular divergence and energy spread of the incident x-ray beam. The high-frequency oscillations apparent at low values of the angular

deviation are thus not observed in the data. The predicted oscillations at angular offsets with a magnitude of more than approximately 0.05°, however, are accurately reproduced in the experimental data.

The three angular settings of the phase plate for the vertical linear polarization and the two circular polarizations are illustrated as dashed lines in Fig. S1. The Poincaré coefficients at these angular settings are: (i) P_L=-0.92, termed π-polarized in the text, (ii) $|P_c|$=0.986 and (iii) $|P_c|$=0.996. Settings (ii) and (iii) represent opposite helicities of circular polarization. The Poincaré coefficients are very close to 1 and are thus assumed to be exactly 1 in the analysis of the magnetic scattering experiments.
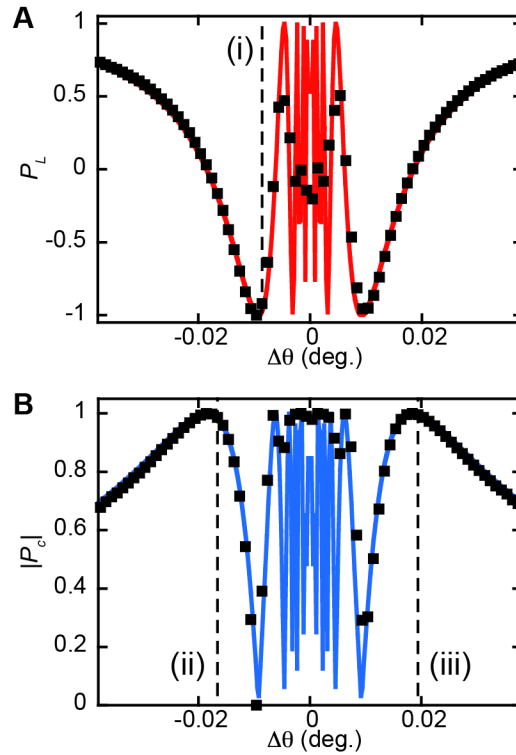

Fig. S1. Measured and simulated Poincaré coefficients of incident x-ray beam. (**A**) Measured (square points) linear and (**B**) circular components of the x-ray radiation after the x-ray phase plate, plotted as a function of the offset between angular setting of the phase plate and the diamond 111 Bragg angle. Vertical lines indicate the angular settings of the phase plate for (i) π linear polarization and (ii) L and (iii) R circular polarizations. The polarization predicted using equations (1a) and (1b) are plotted as solid lines.

Prediction of magnetic diffraction intensity. The intensities of diffracted x-rays from the 008 reflection were predicted for L- and R-circular and π-polarized linear incident polarization using the FDMNES software package. This code can work either using the multiple scattering theory under the muffin-tin approximation on the potential shape, or within the finite difference method with a free shape potential. In the present study, the first approach proved to be sufficient. Simulations were relativistic, including the spin-orbit interaction, and considered both dipole and

quadrupole transition channels. The FDMNES simulations thus incorporate a more comprehensive physical description than analytic formulae, as for example in (*28*).

A first guess of the electronic configuration was obtained by applying the Hund rule. The FDMNES code then solves the Dyson equation to calculate the electronic structure inside a cluster centered on the resonant atom. For the calculation reported here, the cluster had a 5 Å radius and contains 39 atoms. The resonant atomic form factors were then calculated from the electronic structure. The reflection intensities were obtained by considering also the non-resonant magnetic and Thomson terms, taking into account the magnetic space group and the incoming polarization.

The flipping ratios F_{cir} and F_π were calculated from the predicted intensities using the formulas given in the text. The predicted values of F_{cir} and F_π for a range of photon energies spanning the Gd L_2 edge are shown in Fig. 3b of the text and Fig. S2, respectively.
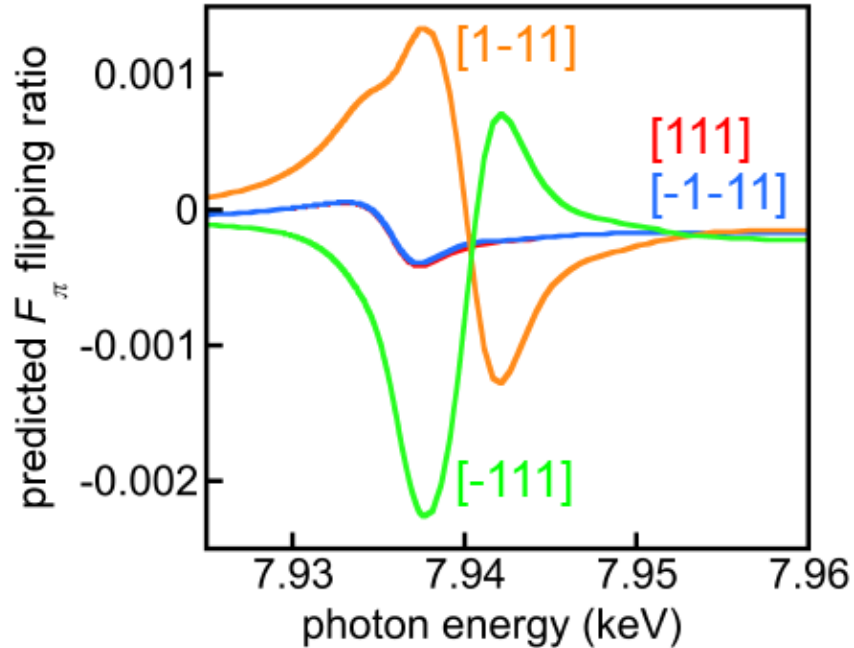

Fig. S2. Predicted flipping ratios for π polarization. Predicted values of the π-polarization flipping ratio F_π as a function of incident photon energy.

Absence of Magnetic Contrast with Linear σ Incident Polarization. Magnetic scattering contrast is not apparent in maps collected with σ linear incident polarization, in which the linear polarization is in the plane of the sample surface. A σ-polarized incident x-ray beam was prepared by setting the diamond phase plate offset angle $\Delta\theta$ to -0.86°. Under these conditions the Poincaré coefficients given by extrapolating from Fig. S1 are $P_L\approx1$ and $|P_c|=0$, corresponding to σ polarization. The maps of the diffracted intensity acquired with σ polarization were analyzed using a flipping ratio defined as $F_\sigma = \frac{I_\sigma - \alpha(I_L + I_R)}{\beta(I_L + I_R)}$. The factors α and β are given in the main text and correct the intensities I_L and I_R accounting for the Lorentz polarization factor in the total intensity.

Maps of the total intensity, F_{cir}, F_π, and F_σ acquired at a photon energy of 7.938 keV are shown in Figs. 3A to D for a region near the edge of the lithographically defined GdIG feature. Maps of F_{cir} and F_π have magnetic contrast with a magnitude similar to the maps shown in Figs. 2 and 3. This contrast is absent in the image in Fig. S3D of the σ-polarization flipping ratio F_σ. The point-to-point variation of F_σ is smaller than for F_{cir} and F_π and exhibits contrast corresponding to the noise in the x-ray measurement, with no correlation to the magnetic features.
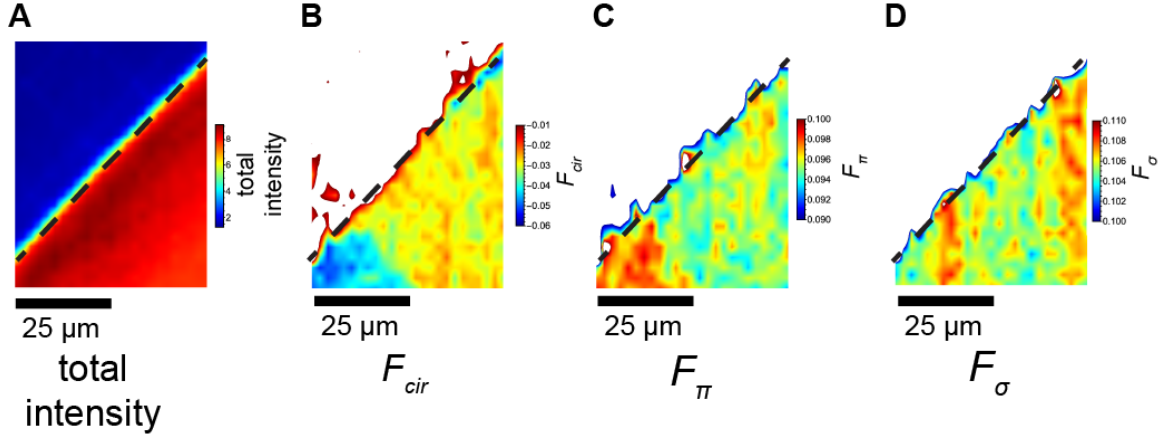

Fig. S3. Maps of total intensity and F_{cir}, F_π, and F_σ flipping ratios. Nanobeam diffraction maps of the edge of a patterned GdIG region in which the GdIG layer is present below the dashed line. (**A**) Total intensity, sum of images acquired with L and R incident polarization, and flipping ratios (**B**) F_{cir}, (**C**) F_π, and (**D**) F_σ.

Free energy analysis and domain-wall energy calculation. The total magnetic anisotropy energy density of the (001)-oriented GdIG thin film f_{tot} is the sum of the magnetocrystalline anisotropy energy density f_{anis}, the magnetic shape anisotropy energy density f_{shape}, the magnetoelastic energy density f_{melast}, and the elastic energy density f_{elast} (43). Specifically, $f_{anis} = K_1(m_1^2 m_2^2 + m_2^2 m_3^2 + m_3^2 m_1^2) + K_2 m_1^2 m_2^2 m_3^2$ with the 1st and 2nd order cubic anisotropy constants K_1 and K_2, respectively, and $f_{shape} = 0.5\mu_0 M_s^2 m_3^2$ with the saturation magnetization M_s. Here $(m_1, m_2, m_3) = (\sin\theta\cos\varphi, \sin\theta\sin\varphi, \cos\theta)$ are the directional cosines of the magnetization defined in the crystallographic reference system using the angles defined in the inset of Fig. S4A. The cubic anisotropy constants at 5 K are $K_1 = -2.164\times10^4 J/m^3$, $K_2 = (0\pm0.9)\times10^3 J/m^3$ (44), μ_0 is the vacuum permeability, and $M_s = 5.52\times10^5$ A/m (4). The energy densities f_{melast} and f_{elast} can be expressed as:

$$f_{melast} = B_1\left[e_{11}\left(m_1^2 - \frac{1}{3}\right) + e_{22}\left(m_2^2 - \frac{1}{3}\right) + e_{33}\left(m_3^2 - \frac{1}{3}\right)\right]$$

$$+ B_2(2m_1 m_2 e_{12} + 2m_1 m_3 e_{13} + 2m_2 m_3 e_{23}) \tag{1}$$

$$f_{elast} = \frac{1}{2}c_{11}(e_{11}^2 + e_{22}^2 + e_{33}^2) + c_{12}(e_{11}e_{22} + e_{22}e_{33} + e_{11}e_{33})$$

$$+ 2c_{44}(e_{12}^2 + e_{23}^2 + e_{13}^2) \tag{2}$$

The magnetoelastic coupling coefficients at ~5 K are: $B_1 = -1.5\lambda_{100}(c_{11}-c_{12}) = -1.659\times10^6$ J/m³ and $B_2 = -3\lambda_{111}c_{44} = 9.181\times10^5$ J/m³. The elastic stiffness coefficients are $c_{11} = 2.731\times10^{11}$ Pa, $c_{12} = 1.250\times10^{11}$ Pa and $c_{44} = 0.741\times10^{11}$ (45). The anisotropic magnetostriction coefficients are

λ_{100} = 7.47×10^{-6} and λ_{111} = -4.13×10^{-6} (*46*). The elastic stiffness and the magnetostriction coefficients are reported from measurements at 4.2 K using GdIG single crystals. From $\sigma_{i3} = 0$ (the condition of stress-free surfaces) and the magnetoelastic equation of state $\sigma_{i3} = \partial(f_{\text{melast}} + f_{\text{elast}})/\partial e_{i3}$ (i = 1,2,3), one can derive $e_{33} = \frac{B_1 - 3c_{12}(e_{11}+e_{22}) - 3B_1 m_3^2}{3c_{11}}$, $e_{13} = -\frac{B_2 m_1 m_3}{2c_{44}}$ and $e_{23} = -\frac{B_2 m_2 m_3}{2c_{44}}$. Plugging in the expressions of e_{i3} into Eqs. (1) and (2), omitting all terms that are independent of m_i (i=1,2,3), one has, (*47, 48*)

$$\Delta f_{\text{tot}}(m_1, m_2, m_3) = B_1(e_{11}m_1^2 + e_{22}m_2^2) + \left[\frac{1}{2}\mu_0 M_s^2 + \frac{B_1^2}{3c_{11}} - \frac{B_1 c_{12}}{c_{11}}(e_{11}+e_{22})\right]m_3^2$$

$$+K_1 m_1^2 m_2^2 + \left(K_1 - \frac{B_2^2}{2c_{44}}\right)(m_1^2 + m_2^2)m_3^2$$

$$+K_2 m_1^2 m_2^2 m_3^2 - \frac{B_1^2}{c_{11}}m_3^4 \tag{3}$$

Minimizing Eq. (3) with respect to m_i (or equivalently the angles θ and φ) allows us to determine the global and local energy minima under biaxial in-plane strains e_{11}, e_{22}, and e_{12}. Assuming that the 21-nm-thick (001) GdIG film is coherently strained by the cubic (001)-oriented GGG substrate, one has $e_{11} = e_{22} = $ -9.636×10^{-3}, calculated from the experimentally measured out-of-plane lattice mismatch. Due to the epitaxial growth of GdIG on GGG, we do not expect any shear strain in the film plane ($e_{12} = 0$).

A plot of f_{tot} as a function of θ and φ is shown in Fig. S4A. The magnetic easy axis of the film is predicted by minimizing f_{tot}, as shown in Figs. 4A and B (*49*). The large saturation magnetization of GdIG at low temperature causes the demagnetization term $\frac{1}{2}\mu_0 M_s^2 m_3^2$, to be dominant, favoring in-plane magnetization, i.e. a magnetically easy (001)-plane. This is despite the fact that the biaxial compressive in-plane lattice mismatch strains ($e_{11} = e_{22} < 0$) favors a perpendicular magnetization along the [001] or [00-1] directions via the finite magnetoelastic coupling.

The anisotropy obtained from Eq. (3) and shown in Figs. S4A and B predicts that GdIG thin films have an in-plane magnetic easy axis. Based on this prediction, it is reasonable to assume that the in-plane boundary oriented along <110> boundary, as in Fig. 4B, is a 180° Néel wall, across which magnetization rotates, for instance, from [110] to [$\bar{1}\bar{1}$0]. If the films were isotropic with respect to in-plane magnetization, the magnetization rotation could occur along any direction in the (110) plane. However, due to the predicted four-fold in-plane magnetic anisotropy (Fig. S4B), caused by the magnetocrystalline anisotropy, the total energy will be minimized when the propagation vector of magnetization rotation is along one of the four in-plane easy directions, such as k_1 ([1$\bar{1}$0]).

The energy density of a 180° Néel wall is given by (*50*):

$$\sigma^{180} = 2\sqrt{A} \int_0^\pi \sqrt{g(\beta)}\,d\beta$$

$$g(\beta) = \Delta f_{\text{tot}}(m_1', m_2', m_3')$$

Here (m_1', m_2', m_3') are the direction cosines of the magnetization defined in the crystallographic reference system and can be expressed using angles α and β. Here $m_i' = R_{ij}m_j$ $(i, j=1,2,3)$, where the rotation matrix R_{ij} depends on α:

$$R_{rotate}(\alpha) = \begin{bmatrix} \frac{\sqrt{2}}{2}\cos\alpha & \frac{\sqrt{2}}{2} & \frac{\sqrt{2}}{2}\sin\alpha \\ -\frac{\sqrt{2}}{2}\cos\alpha & \frac{\sqrt{2}}{2} & -\frac{\sqrt{2}}{2}\sin\alpha \\ -\sin\alpha & 0 & \cos\alpha \end{bmatrix}$$

while $(m_1, m_2, m_3) = (\sin\beta, \cos\beta, 0)$ for a 180° Néel wall. The isotropic exchange coefficient A only influences the absolute magnitude of the wall energy density.

The 90° Néel wall energy density is half of that for a 180° Néel wall. Thus, its energetically favorable propagation vector should likewise follow one of the four easy in-plane directions such as k_1. For example, consider that magnetization rotates from [110] by 90° to [1$\bar{1}$0] with a propagation vector along [1$\bar{1}$0] as well, the 90° Néel wall boundary should then be 45° with respect to both [110] and [1$\bar{1}$0], that is, the [100] direction.

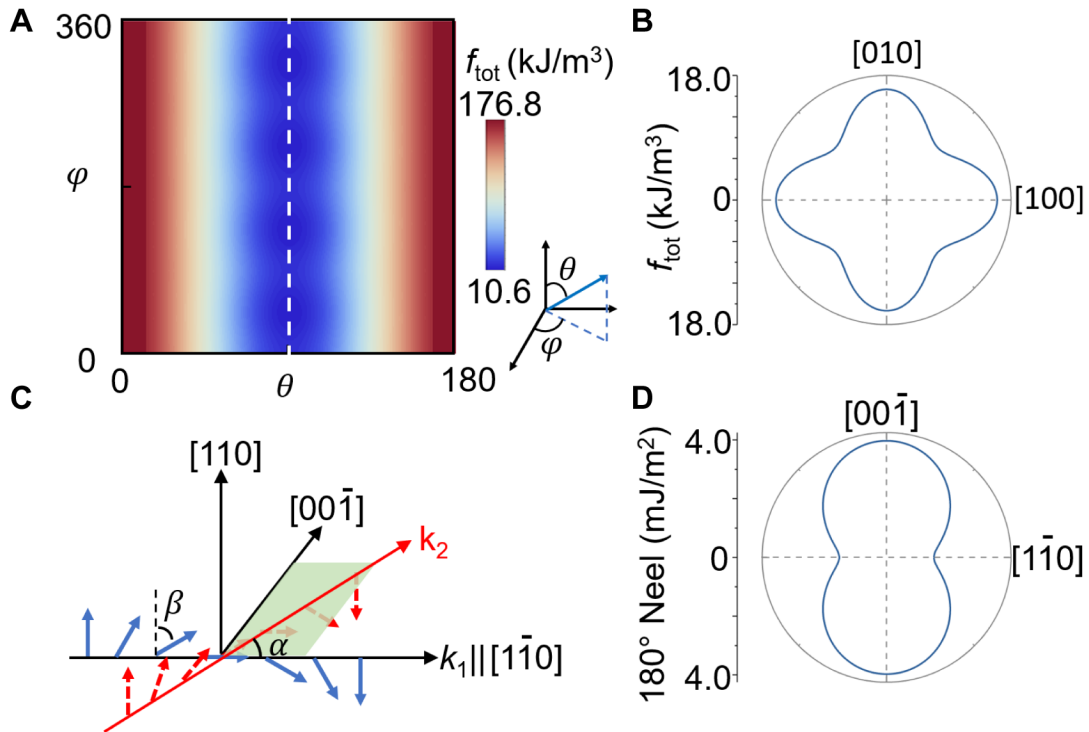**Fig. S4. Magnetic model.** (**A**) Magnetic anisotropy energy density f_{tot} of the (001) GdIG thin film as a function of the azimuth angles θ and φ defined in the inset. (**B**) Variation of f_{tot} as a function of φ for in-plane magnetization (i.e. with θ=90°). (**C**) Schematic of a 180° Néel Wall with an in-plane [110] boundary. The local magnetization (red or blue arrows) varies cycloidally across the [110] boundary. α is defined the angle between the propagation vector k_2 and [1-10] and β is the angle between the local magnetization and the [110] boundary. (**D**) Calculated 180° Néel wall energy density as a function of the propagation vector direction parameterized by the angle α.

REFERENCES AND NOTES

1. S. A. Wolf, D. D. Awschalom, R. A. Buhrman, J. M. Daughton, S. von Molnár, M. L. Roukes, A. Y. Chtchelkanova, D. M. Treger, Spintronics: A spin-based electronics vision for the future. *Science* **294**, 1488–1495 (2001).

2. S. I. Kiselev, J. C. Sankey, I. N. Krivorotov, N. C. Emley, R. J. Schoelkopf, R. A. Buhrman, D. C. Ralph, Microwave oscillations of a nanomagnet driven by a spin-polarized current. *Nature* **425**, 380–383 (2003).

3. G. E. W. Bauer, E. Saitoh, B. J. van Wees, Spin caloritronics. *Nat. Mater.* **11**, 391–399 (2012).

4. S. Geprägs, A. Kehlberger, F. Della Coletta, Z. Qiu, E.-J. Guo, T. Schulz, C. Mix, S. Meyer, A. Kamra, M. Althammer, H. Huebl, G. Jakob, Y. Ohnuma, H. Adachi, J. Barker, S. Maekawa, G. E. W. Bauer, E. Saitoh, R. Gross, S. T. B. Goennenwein, M. Kläui, Origin of the spin Seebeck effect in compensated ferrimagnets. *Nat. Commun.* **7**, 10452 (2016).

5. G. J. Snyder, E. S. Toberer, Complex thermoelectric materials. *Nat. Mater.* **7**, 105–114 (2008).

6. R. Venkatasubramanian, E. Siivola, T. Colpitts, B. O'Quinn, Thin-film thermoelectric devices with high room-temperature figures of merit. *Nature* **413**, 597–602 (2001).

7. K. Uchida, S. Takahashi, K. Harii, J. Ieda, W. Koshibae, K. Ando, S. Maekawa, E. Saitoh, Observation of the spin Seebeck effect. *Nature* **455**, 778–781 (2008).

8. K.-i. Uchida, T. Nonaka, T. Ota, E. Saitoh, Longitudinal spin-Seebeck effect in sintered polycrystalline (Mn, Zn) Fe_2O_4. *Appl. Phys. Lett.* **97**, 262504 (2010).

9. J. Xiao, G. E. W. Bauer, K.-i. Uchida, E. Saitoh, S. Maekawa, Theory of magnon-driven spin Seebeck effect. *Phys. Rev. B* **81**, 214418 (2010).

10. E. Saitoh, M. Ueda, H. Miyajima, G. Tatara, Conversion of spin current into charge current at room temperature: Inverse spin-Hall effect. *Appl. Phys. Lett.* **88**, 182509 (2006).

11. J. Cramer, E.-J. Guo, S. Geprägs, A. Kehlberger, Y. P. Ivanov, K. Ganzhorn, F. Della Coletta, M. Althammer, H. Huebl, R. Gross, J. Kosel, M. Kläui, S. T. B. Goennenwein, Magnon mode selective spin transport in compensated ferrimagnets. *Nano Lett.* **17**, 3334–3340 (2017).

12. I. Gray, T. Moriyama, N. Sivadas, G. M. Stiehl, J. T. Heron, R. Need, B. J. Kirby, D. H. Low, K. C. Nowack, D. G. Schlom, D. C. Ralph, T. Ono, G. D. Fuchs, Spin Seebeck imaging of spin-torque switching in antiferromagnetic Pt/NiO heterostructures. *Phys. Rev. X* **9**, 041016 (2019).

13. J. F. K. Cooper, C. J. Kinane, S. Langridge, M. Ali, B. J. Hickey, T. Niizeki, K. Uchida, E. Saitoh, H. Ambaye, A. Glavic, Unexpected structural and magnetic depth dependence of YIG thin films. *Phys. Rev. B* **96**, 104404 (2017).

14. J. Mendil, M. Trassin, Q. Bu, J. Schaab, M. Baumgartner, C. Murer, P. T. Dao, J. Vijayakumar, D. Bracher, C. Bouillet, C. A. F. Vaz, M. Fiebig, P. Gambardella, Magnetic

properties and domain structure of ultrathin yttrium iron garnet/Pt bilayers. *Phys. Rev. Mater.* **3**, 034403 (2019).

15. M. Kubota, A. Tsukazaki, F. Kagawa, K. Shibuya, Y. Tokunaga, M. Kawasaki, Y. Tokura, Stress-induced perpendicular magnetization in epitaxial iron garnet thin films. *Appl. Phys. Exp.* **5**, 103002 (2012).

16. A. M. Kalashnikova, V. V. Pavlov, A. V. Kimel, A. Kirilyuk, T. Rasing, R. V. Pisarev, Magneto-optical study of holmium iron garnet $Ho_3Fe_5O_{12}$. *Low Temp. Phys.* **38**, 863–869 (2012).

17. R. W. Hansen, L. E. Helseth, A. Solovyev, E. Il'Yashenko, T. H. Johansen, Growth and characterization of (100) garnets for imaging. *J. Magnet. Magnet. Mater.* **272-276**, 2247–2249 (2004).

18. P. G. Evans, E. D. Isaacs, G. Aeppli, Z. Cai, B. Lai, X-ray microdiffraction images of antiferromagnetic domain evolution in chromium. *Science* **295**, 1042–1045 (2002).

19. T. Higo, H. Man, D. B. Gopman, L. Wu, T. Koretsune, O. M. J. van't Erve, Y. P. Kabanov, D. Rees, Y. Li, M.-T. Suzuki, S. Patankar, M. Ikhlas, C. L. Chien, R. Arita, R. D. Shull, J. Orenstein, S. Nakatsuji, Large magneto-optical Kerr effect and imaging of magnetic octupole domains in an antiferromagnetic metal. *Nat. Photonics* **12**, 73–78 (2018).

20. J. Li, J. Pelliciari, C. Mazzoli, S. Catalano, F. Simmons, J. T. Sadowski, A. Levitan, M. Gibert, E. Carlson, J.-M. Triscone, S. Wilkins, R. Comin, Scale-invariant magnetic textures in the strongly correlated oxide $NdNiO_3$. *Nat. Commun.* **10**, 4568 (2019).

21. S.-W. Cheong, M. Fiebig, W. Wu, L. Chapon, V. Kiryukhin, Seeing is believing: Visualization of antiferromagnetic domains. *npj Quantum Mater.* **5**, 3 (2020).

22. M. Seul, L. R. Monar, L. O'Gorman, R. Wolfe, Morphology and local structure in labyrinthine stripe domain phase. *Science* **254**, 1616–1618 (1991).

23. H. Maier-Flaig, S. Geprägs, Z. Qiu, E. Saitoh, R. Gross, M. Weiler, H. Huebl, S. T. B. Goennenwein, Perpendicular magnetic anisotropy in insulating ferrimagnetic gadolinium iron garnet thin films. arXiv:1706.08488 [cond-mat.mtrl-sci] (2017).

24. E. R. Rosenberg, L. Beran, C. O. Avci, C. Zeledon, B. Song, C. Gonzalez-Fuentes, J. Mendil, P. Gambardella, M. Veis, C. Garcia, G. S. D. Beach, C. A. Ross, Magnetism and spin transport in rare-earth-rich epitaxial terbium and europium iron garnet films. *Phys. Rev. Mater.* **2**, 094405 (2018).

25. S. B. Ubizskii, Orientational states of magnetization in epitaxial (111)-oriented iron garnet films. *J. Magnet. Magnet. Mater.* **195**, 575–582 (1999).

26. S. M. Aliev, I. K. Kamilov, M. S. Aliev, Z. G. Ibaev, A study of the domain structure of ferrites in the vicinity of the compensation point by Mössbauer spectroscopy. *Tech. Phys. Lett.* **42**, 118–120 (2016).

27. T. Yoshimoto, T. Goto, K. Shimada, B. Iwamoto, Y. Nakamura, H. Uchida, C. A. Ross, M. Inoue, Static and dynamic magnetic properties of single-crystalline yttrium iron garnet films epitaxially grown on three garnet substrates. *Adv. Electron. Mater.* **4**, 1800106 (2018).

28. D. Haskel, E. Kravtsov, Y. Choi, J. C. Lang, Z. Islam, G. Srajer, J. S. Jiang, S. D. Bader, P. C. Canfield, Charge-magnetic interference resonant scattering studies of ferromagnetic crystals and thin films. *Euro. Phys. J. Spec. Top.* **208**, 141–155 (2012).

29. Y. Sasaki, M. Okube, S. Sasaki, Resonant and non-resonant magnetic scatterings with circularly polarized x-rays: Magnetic scattering factor and electron density of gadolinium iron garnet. *Acta Cryst. A* **73**, 257–270 (2017).

30. C. Donnelly, M. Guizar-Sicairos, V. Scagnoli, S. Gliga, M. Holler, J. Raabe, L. J. Heyderman, Three-dimensional magnetization structures revealed with x-ray vector nanotomography. *Nature* **547**, 328–331 (2017).

31. O. Bunău, Y. Joly, Self-consistent aspects of x-ray absorption calculations. *J. Phys. Condens. Matter* **21**, 345501 (2009).

32. P. G. Evans, D. E. Savage, J. R. Prance, C. B. Simmons, M. G. Lagally, S. N. Coppersmith, M. A. Eriksson, T. U. Schulli, Nanoscale distortions of Si quantum wells in Si/SiGe quantum-electronic heterostructures. *Adv. Mater.* **24**, 5217–5221 (2012).

33. E. A. Giess, D. C. Cronemeyer, Magnetic anisotropy of $Eu_{0.65}Y_{2.35}Fe_{3.8}Ga_{1.2}O_{12}$ films grown on garnet substrates with different lattice parameters. *Appl. Phys. Lett.* **22**, 601–602 (1973).

34. J. Fu, M. Hua, X. Wen, M. Xue, S. Ding, M. Wang, P. Yu, S. Liu, J. Han, C. Wang, H. Du, Y. Yang, J. Yang, Epitaxial growth of $Y_3Fe_5O_{12}$ thin films with perpendicular magnetic anisotropy. *Appl. Phys. Lett.* **110**, 202403 (2017).

35. P. Godard, G. Carbone, M. Allain, F. Mastropietro, G. Chen, L. Capello, A. Diaz, T. H. Metzger, J. Stangl, V. Chamard, Three-dimensional high-resolution quantitative microscopy of extended crystals. *Nat. Commun.* **2**, 568 (2011).

36. K. Shen, Temperature-switched anomaly in the spin Seebeck effect in $Gd_3Fe_5O_{12}$. *Phys. Rev. B* **99**, 024417 (2019).

37. C. O. Avci, E. Rosenberg, L. Caretta, F. Büttner, M. Mann, C. Marcus, D. Bono, C. A. Ross, G. S. D. Beach, Interface-driven chiral magnetism and current-driven domain walls in insulating magnetic garnets. *Nat. Nanotechnol.* **14**, 561–566 (2019).

38. H. Miyagawa, N. Kawamura, M. Suzuki, Temperature dependence of x-ray magnetic circular dichroism in rare earth iron garnets (rare earth = Gd, Dy and Sm). *Phys. Scr.* **2005**, 616 (2005).

39. M. Schreier, N. Roschewsky, E. Dobler, S. Meyer, H. Huebl, R. Gross, S. T. B. Goennenwein, Current heating induced spin Seebeck effect. *Appl. Phys. Lett.* **103**, 242404 (2013).

40. J. C. Lang, G. Srajer, Bragg transmission phase plates for the production of circularly polarized x-rays. *Rev. Sci. Instrum.* **66**, 1540–1542 (1995).

41. J. C. Lang, X. Wang, V. P. Antropov, B. N. Harmon, A. I. Goldman, H. Wan, G. C. Hadjipanayis, K. D. Finkelstein, Circular magnetic x-ray dichroism in crystalline and amorphous GdFe$_2$. *Phys. Rev. B* **49**, 5993–5998 (1994).

42. M. Suzuki, Y. Inubushi, M. Yabashi, T. Ishikawa, Polarization control of an X-ray free-electron laser with a diamond phase retarder. *J. Synchrotron Rad.* **21**, 466–472 (2014).

43. S. Geprägs, A. Brandlmaier, M. S. Brandt, R. Gross, S. T. B. Goennenwein, Strain-controlled nonvolatile magnetization switching. *Solid State Commun.* **198**, 7–12 (2014).

44. B. A. Calhoun, M. J. Freiser, Anisotropy of gadolinium iron garnet. *J. Appl. Phys.* **34**, 1140–1145 (1963).

45. R. L. Comstock, J. J. Raymond, W. G. Nilsen, J. P. Remeika, Spin-wave spectrum of gadolinium iron garnet. *Appl. Phys. Lett.* **9**, 274–276 (1966).

46. A. E. Clark, J. J. Rhyne, E. R. Callen, Magnetostriction of dilute dysprosium iron and of gadolinium iron garnets. *J. Appl. Phys.* **39**, 573–575 (1968).

47. N. A. Pertsev, Giant magnetoelectric effect via strain-induced spin reorientation transitions in ferromagnetic films. *Phys. Rev. B* **78**, 212102 (2008).

48. J.-M. Hu, C. W. Nan, Electric-field-induced magnetic easy-axis reorientation in ferromagnetic/ferroelectric layered heterostructures. *Phys. Rev. B* **80**, 224416 (2009).

49. M. Weiler, A. Brandlmaier, S. Geprägs, M. Althammer, M. Opel, C. Bihler, H. Huebl, M. S. Brandt, R. Gross, S. T. B. Goennenwein, Voltage controlled inversion of magnetic anisotropy in a ferromagnetic thin film at room temperature. *New J. Phys.* **11**, 013021 (2009).

50. B. D. Cullity, C. D. Graham, *Introduction to Magnetic Materials* (John Wiley & Sons, 2011).